

A 3D Segmentation Method for Pulmonary Nodule Image Sequences based on Supervoxels and Multimodal Data

Qiang Cui^a, Zinlin Qiang^a, Juanjuan Zhao^{a,*}, Yan Qiang^a, Xiaolei Liao^a

^a*School of Computer Science and Technology, Taiyuan University of Technology, Taiyuan, 030024, China*

Abstract

Three-dimensional reconstruction can reflect the dynamic relationship between lung lesions and surrounding tissues. It is easy to obtain an intuitive understanding of the shape, size, appearance and surroundings of pulmonary nodules, such as pleura or blood vessels. Three-dimensional reconstruction greatly improves the quality of surgery and reduces risk. This technique can help doctors to understand disease better and can guide operations in complex anatomical areas; therefore, it is worth recommending its clinical use. Therefore, our paper proposes a 3D segmentation method for use with pulmonary nodule image sequences based on supervoxels and multimodal data. First, we segment the lung parenchyma into superpixels. Then, we register PET/CT images using mutual information to roughly locate pulmonary nodule areas, matching the accurate pulmonary nodule areas using a multi-scale circular template matching algorithm. Finally, an improved three-dimensional supervoxel region-growing algorithm is proposed to reconstruct three-dimensional pulmonary nodules. The experimental results show that compared with the 3D region-growing algorithm, our algorithm can reconstruct complex pulmonary nodules more accurately and reduce time complexity.

Keywords: Multimodal data; Pulmonary nodules; Region growing; Supervoxel; Three-dimensional reconstruction

(Submitted on April 20, 2017; Revised on June 13, 2017; Accepted on August 20, 2017)

© 2017 Totem Publisher, Inc. All rights reserved.

1. Introduction

Lung cancer is one of the most common causes of cancer-related death worldwide [29]. With the emergence and development of medical imaging technology, people can image the human body and its internal organs using two-dimensional digital image sequences. Computed tomography (CT) [7] scanning technology provides good density resolution for human lesions and is currently the most effective and direct imaging method for the early diagnosis of lung cancer. Positron Emission Tomography (PET) [4] is a nuclear medicine functional imaging technology that uses the tracer principle to show each organ's tissue metabolism and is the most advanced image detection technology in the field of nuclear medicine.

PET/CT technology [1] fully combines PET functional images and CT structural images and provides information from two kinds of scanning information at the same time, ultimately providing more information than single-scan technology. Providing more accurate positioning of the lesion area on PET/CT images can improve the detection efficiency significantly. The clinical application of these medical imaging techniques has led to great advances in medical diagnosis and treatment techniques. However, despite initiatives to promote early diagnosis, physicians do not always make the best use of the data acquired from imaging devices [22,31]. Two-dimensional tomographic images can only express cross-sectional information; therefore, it is difficult to establish the three-dimensional structure of the lesion area.

This method can improve the scientific accuracy of medical diagnosis and treatment planning. Transforming two-dimensional CT sequence images into an image with an intuitive stereoscopic effect can show the three-dimensional structure and morphology of human organs, thus providing anatomical information that cannot be obtained by traditional methods. In addition, this technique provides a visual interaction method for use in simulating operations. The three-dimensional

* Corresponding author.

E-mail address: zh_juanjuan@126.com

reconstruction and visualization of medical images has been proposed in this context and has been widely researched and used.

A. Farag [10] targeted the processing of CT images by performing the steps of threshold segmentation, modeling and nodule segmentation in two dimensions. S. S. Sun [30] proposed a method based on k-means clustering and flowing entropy combined with geodesic distances to solve the segmentation problem of juxta-vascular nodules, and this method proved effective for complex juxta-vascular nodules. However, the authors only segmented two-dimensional images and did not extend their study to three dimensions; furthermore, they were unable to intuitively display the appearance of the pulmonary nodules and their relationship with surrounding tissues. C. Revol-Muller [28] proposed a set of values termed “the assessment function” to determine an optimal homogeneity criterion, which automatically segmented trabecular bone samples in three-dimensional images using the 3D region-growing method. However, region growing acts at the pixel level, resulting in high complexity and requiring lengthy times. W. Wu [35] proposed a novel transform method for the automatic delineation of liver on CT volume images using supervoxel-based graph cuts; this method detected the liver accurately with significantly reduced processing time. B. Irving [15] proposed a novel method for tumor detection based on signal enhancement characteristics, which automatically segmented a colorectal tumor in DCE-MRI using supervoxel neighborhood contrast characteristics to reduce the time complexity. S. Wu and J. Wang [34] described a method that recognizes nodules based on 3D geometric information through the processes of interpolation, segmentation, and suspicious area searching and recognition for automatic nodule detection on serial CT scans based on their shape features. T. W. Way [33] developed a computer-aided diagnosis system to segment the nodule from its surrounding structured background in a local volume of interest and extract image features for classification. Image segmentation was performed using a three-dimensional active contour method. However, the authors did not consider the characteristics of the tumor itself; therefore, the reconstruction results were not very precise. S. Kobashi [16] proposed a method for cerebral vascular segmentation based on a neural network. Blood vessels were binarized according to a user-selected threshold and were segmented using a watershed method, which segmented the cerebral vascular system using a neural network algorithm. The method did not require too much artificial intervention; however, the large number of neural network parameters, high complexity, and long training time rendered it difficult to segment small branches.

Most literature reports have focused on two-dimensional images or liver and brain image segmentation algorithms, but the segmentation method used for pulmonary nodules only shows information on one slice of lung parenchyma. In practical applications, to understand and diagnose lung images better, it is necessary to include information on nodule size, location, and direction and their relationship with surrounding tissues. Therefore, it is important to study the application of segmentation algorithms to three-dimensional pulmonary nodule images. In view of the above problems, our paper proposes a 3D supervoxel pulmonary nodule segmentation method based on multimodal sequence lung image data that fully combines lung lesion information provided by PET/CT image data. Experiments show that our method can significantly reduce time complexity and improve the accuracy of segmentation and reconstruction.

2. Method

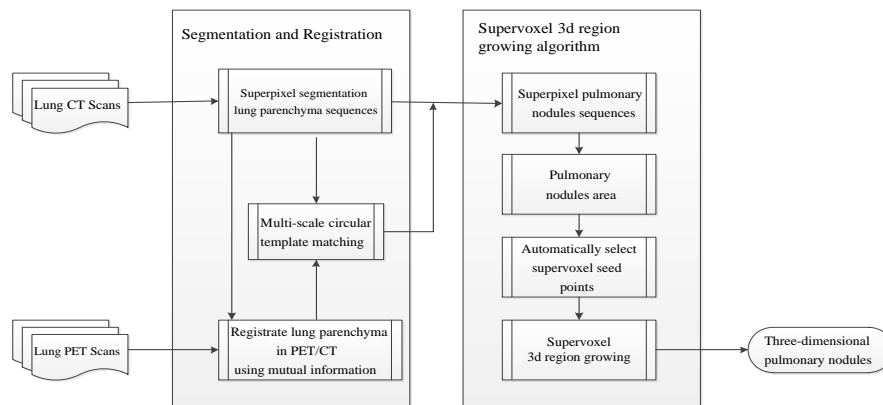


Figure 1. The generation of pulmonary nodule image sequences.

We propose a complete segmentation method for use with pulmonary nodules in PET/CT image sequences; this method is based on the lung parenchyma results obtained in our previous work [18] using a cluster of supervoxels with a self-generating neural forest to obtain lung parenchyma image sequences. Our method uses these lung parenchyma results to register PET/CT images based on mutual information and then uses a multi-scale circular template matching algorithm to obtain accurate

nodule areas. We then select a seed point automatically and design the growth criteria for improved supervoxel 3D region-growing to reconstruct 3D pulmonary nodules. A diagram of our proposed method is shown in Figure 1.

2.1. Superpixel Segmentation for Use with Lung Parenchyma

Our previous method [18] used the position of lung parenchyma image features to obtain lung parenchyma ROI image sequences. A gradient and sequential linear iterative clustering algorithm for sequence image segmentation is then proposed to segment the ROI image sequences and obtain superpixel samples. The SGNF, which is optimized by a genetic algorithm, is then utilized for superpixel clustering. Finally, the gray and geometric features of the superpixel samples are used to identify and segment all the lung parenchyma image sequences. A result showing lung parenchyma image sequences segmented by superpixels is shown in Figure 2.

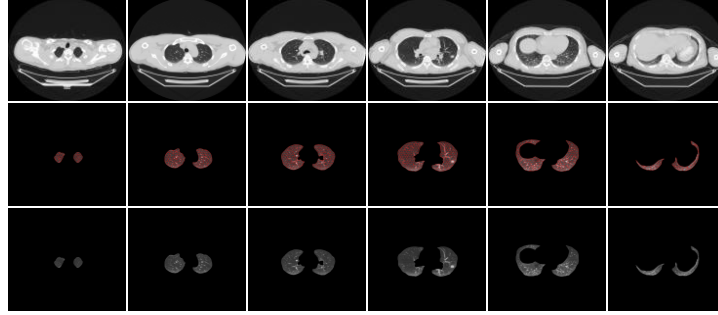


Figure 2. Segmentation results for lung parenchyma image sequences.

Because of the large number of image sequences, we selected six lung CT images from the top to the bottom of the lung in our dataset (first row in Figure 2) and then used one image out of every thirteen to demonstrate the process and the results of lung image segmentation. The second row in Figure 2 shows the results of lung parenchyma based on superpixels with a self-generating neural forest. The third row in Figure 2 shows the final lung parenchyma result. Our method is based on these lung parenchyma results and enables the segmentation and reconstruction of pulmonary nodules.

2.2. PET/CT Registration based on Mutual Information

The registration of multimodal images of the same subject provides a way of fusing different types of information and is very important for medical diagnosis and computer-aided surgery [23]. Multimodal registration methods include CT-MRI, CT-PET, PET-MRI, PET-US, and US-CT.

Mutual information (MI), which measures the statistical dependency between two images, has been successfully applied to multimodal image registration. P. Viola [32] first used mutual information as a similarity measure for image registration issues. For two random variables A and B with entropies $H(A)$, $H(B)$, and $H(A,B)$ and probability distributions $P_A(a)$ and $P_B(b)$, their mutual information $MI(A, B)$ is defined according to (1).

$$MI(A, B) = H(A) + H(B) - H(A, B) = \sum_{a,b} P_{AB}(a, b) \cdot \log \frac{P_{AB}(A, B)}{P_A(A) \cdot P_B(b)} \quad (1)$$

MI is an image similarity measure that is widely used in medical image registration. Two images being registered can be considered as two random variable sets of the images' gray scale values; for the floating image A and the reference image B , a and b are the gray values of voxels associated with the two images and are connected by coordinate transformation. Their edge probability distributions and joint probability distributions $P_A(a)$, $P_B(b)$ and $P_{AB}(a, b)$ are the probabilities of having gray-scale values a and b in the image. When the two images reach the best registration position, $MI(A, B)$ reaches its maximum value [21]. The MI registration method is recognized as one of the best retrospective registration methods for registration accuracy and robustness. We use the MI registration method to obtain the approximate location of the nodules.

To eliminate the influence of active regions such as the heart on the results of the experiment, we used lung parenchyma results to register the images, as shown in Figure 3.

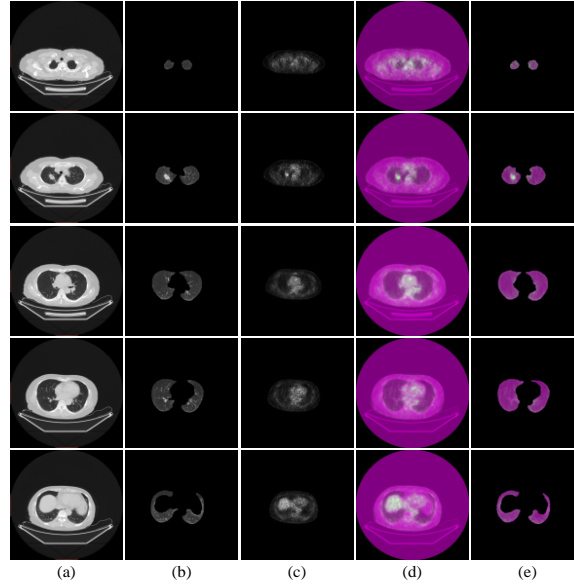


Figure 3. The registration results of PET/CT images based on MI for lung parenchyma image sequences. Column (a) shows five original lung CT images from top to the bottom. Column (b) shows the segmentation results for the lung parenchyma shown in (a). Column (c) shows the interpolation results for the PET images shown in (a). Column (d) shows the results of registration based on the MI of (a). Column (e) shows the results of registration based on MI for the lung parenchyma images shown in (b).

Because the PET image size is 128×128 but the CT image size is 512×512 , we used a linear interpolation method to expand the PET images to 512×512 so that they could be registered with the CT images.

2.3. Multi-scale Circular Template Matching Algorithm

Template matching algorithm is a digital image processing technique for finding small parts of an image that match a template image [3]. This technique can be used to detect edges for image registration [19].

Our paper proposes a template matching method to accurately search for nodule regions based on the approximate results obtained using MI registration. Because the pulmonary nodules are surrounded by lung tissues, they are similarly circular in shape. Therefore, we selected a circular template.

Standardized Uptake Value (SUV) is most commonly used semi-quantitative parameter for analyzing PET images in routine clinical practice.

PET images are stored as DICOM files [2]. DICOM files are the main source used to analyze and calculate SUV. These files can be divided into two parts: the image and metadata. The image displays the image information, and the metadata saves data such as injection dose, type of scan, patient weight, patient name, etc. SUV in DICOM are calculated as shown in (2).

$$SUV_{bodyweight(kg/ml)} = \frac{tissue\ concentration_{(Bq/ml)}}{\left(\frac{injected\ dose_{(Bq)}}{body\ weight_{(kg)}} \right)} \quad (2)$$

In humans, different organs have different levels of metabolism. Usually, the heart, brain, blood vessels, and kidneys have a higher metabolism. In the same organ, tumors generally have a higher metabolism, and this feature is used for the diagnosis of cancer.

SUV are widely used to distinguish between malignant and benign tumors. The mean SUV is better able to reflect whether the region contains pulmonary nodules. Experiments show that when the mean SUV is 2.5 or greater in the lung parenchyma region [24], we can determine that the tumor area is located in the pulmonary nodule area. Thus, we chose an SUV of 2.5 as our criterion for the diagnosis of pulmonary nodules.

To improve the efficiency of the algorithm, we proposed a multi-scale circular template matching algorithm. Initially, a large circular template is used to located nodule's position; a small template is then used to determine the edge information of the nodules. Using a large template, the smallest nodules will occupy approximately 1/40 of the area of the template, and the largest nodules will occupy approximately 1/4 of the area of the template. To ensure that the smallest nodules will be found by calculating the SUVs for normal tissues of lung PET images, we chose an SUV threshold in the initial template of 1.5 to ensure the sensitivity of the template.

The parameters were set as follows: the radius of the template = T_i . Initial threshold = S . Minimum template radius $T_{min} = 3$ mm. Maximum SUV threshold $SUV_{max} = 3.0$. Initial template radius $T_l = 30$ mm (a pulmonary nodule is defined as a focal opacity with a diameter between 3 and 30 mm [13]). Initial threshold $S = 1.5$. Traversing the parenchyma image, the moving distance is equal to the radius of the circle T_i . The mean SUV of the template is calculated; if SUV_{mean} is greater than 2.5, then the area is marked as a pulmonary nodule area. If the area $SUV_{mean} > S$ and < 2.5 , then (3) is used to calculate a smaller radius template to continue the assessment. If the $SUV_{mean} > 2.5$ in the smaller template, then this area is marked as a pulmonary nodule area. Template matching is ended when T_i reaches the minimum value T_{min} . The whole area of the lung parenchyma image is traversed, and the pulmonary nodules are located directly in the lung parenchyma. A schematic diagram of the multi-scale circular template matching algorithm is shown in Figure 4. The results obtained using the multi-scale circular template matching algorithm is shown in Figure 5. The multi-scale circular template matching algorithm is shown in Algorithm 1.

$$T_{i+1} = T_i \cdot \left(\frac{SUV_{mean}}{SUV_{max}} \right)^2 \quad (3)$$

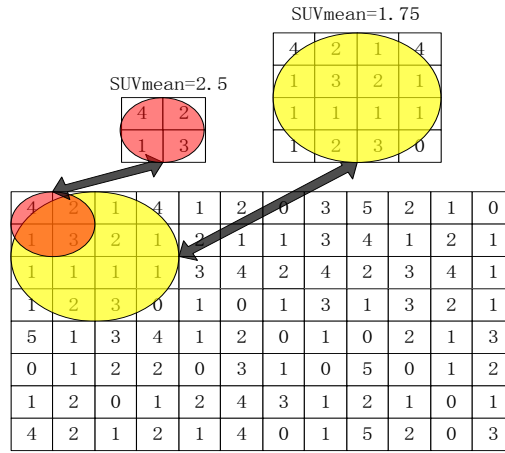


Figure 4. Diagram of multi-scale circular template matching algorithm.

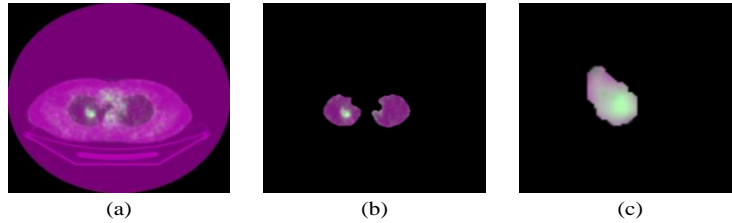


Figure 5. The results obtained using the multi-scale circular template matching algorithm. (a) shows the results of registration based on the MI of the original lung CT images; (b) shows the results of registration for lung parenchyma images; and (c) shows the nodule results area obtained using the circular template matching algorithm shown in (b).

We obtain the pulmonary nodule area after using the multi-scale circular template matching algorithm; then, we compare the results with the area of lung parenchyma we previously obtained. Thus, we can obtain the sequence of pulmonary nodules, which were segmented by superpixels, whereby an accurate pulmonary nodule profile can be obtained. We then perform an AND operation with the original CT and finally obtain the accurate pulmonary nodule area. The experimental procedure is shown in Figure 6.

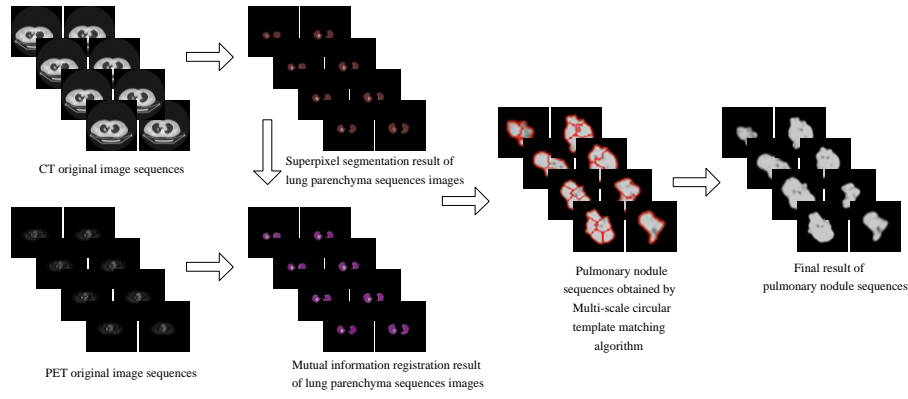


Figure 6. Experimental flow.

Algorithm 1 Multi-scale circular template matching algorithm

1. Set the initial template radius $T_l = 30$ mm, threshold $S = 1.5$;
2. Use a circular template with radius T_l , and obtain a match with the origin points of the input image;
3. Calculate SUV_{mean} using the circular template; if SUV_{mean} is greater than 2.5 go to 6; otherwise, go to 4;
4. If $SUV_{mean} > S$ & < 2.5 in the template, then calculate T_{i+1} , generate a smaller template with new radius, and go to 3;
5. Repeat steps 3-4 until $T_i = T_{min}$ or obtain a template match;
6. Mark the area as a pulmonary nodule area; move the template a distance of T_i mm, and go to 3;
7. Repeat steps 2-6 until all sequences in the PET images are matched.

2.4. Improved Supervoxel 3D Region-growing Method

The concept of supervoxels was first put forward by X. Ren [27] in 2003. A supervoxel is a collection of pixels with similar characteristics such as color, brightness, and texture. An image can be composed of a certain number of supervoxels that contain multiple combinations of pixel characteristics and can preserve the edge information of the original image. Compared with a single pixel, a supervoxel contains rich characteristic information and can greatly reduce image processing complexity and significantly increase the speed of image segmentation. Traditional supervoxel segmentation uses a simple linear iterative clustering (SLIC) process and, when improved by G. H. Gu, A. A. Hammoudi, M. Liu and A. Moore [11,12,20,25], it was applied to single image segmentation. Y. Chen, J. H. Chu [5,6] applied this method to medical images.

In SLIC, each pixel in the sequence of lung CT images can be represented by a five-dimensional feature vector $([l, a, b, x, y]^T)$. The similarity between the pixels can be measured by the Euclidean distance between them. A pixel's feature vector comprises its color vector $[l, a, b]$ in CIELAB color space and its space coordinate vector $[x, y]$, where x and y are the pixel coordinates. An original CT image with N pixels is divided into K supervoxels, and each supervoxel contains approximately N/K pixels; therefore, the average length of each supervoxel S is approximately $\sqrt{N/K}$. Taking one cluster center for every S pixels and taking a $2S \times 2S$ distance around this cluster center as the search space, a search for similar pixels is performed.

In SLIC, the similarity of D_s between the pixels can be calculated based on their color feature distance D_{lab} and their space feature distance D_{xy} . The formulae used to calculate D_{lab} , D_{xy} and D_s are as follows (4-6):

$$D_{lab} = \sqrt{(l_j - l_i)^2 + (a_j - a_i)^2 + (b_j - b_i)^2} \quad (4)$$

$$D_{xyz} = \sqrt{(x_j - x_i)^2 + (y_j - y_i)^2} \quad (5)$$

$$D_s = \frac{D_{lab} + \alpha D_{xy}}{\sqrt{1 + \alpha^2}} \quad (6)$$

In these formulae, i is the i -th super-pixel clustering center, j represents a pixel in the search area, and α is a parameter used to adjust the weight of D_{lab} and D_{xy} .

In this paper, we extend the concept of a two-dimensional superpixel to a three-dimensional supervoxel. A supervoxel is a collection of voxels with similar characteristics, and a 3D image can comprise several supervoxels. Supervoxels contain multiple combinations of the voxel characteristics and can preserve the edge information of the original image; they may also contain abundant characteristic information and can include statistical information relating to many individual voxels.

Because medical images are grayscale images, we only use L in CIELAB color space and its 3D space coordinate vector $[x, y, z]$, where x and y are the pixel coordinates, and z is the serial number of the image; the SUV value w is used for the current coordinates of PET images. This five-dimensional feature vector $[l, x, y, z, w]^T$ is used to represent every supervoxel.

In our method, for original CT image sequences with M voxels that needs to be divided into L supervoxels, each supervoxel contains approximately M/L voxels. Taking a cluster center between every S voxel and taking $2S \times 2S \times 2S$ distance around this cluster center as its search space, a search for similar voxels is conducted. The similarity between two voxels in sequence images D_s can be calculated based on their color feature distance D_l , space feature distance D_{xyz} , and the SUV difference D_w between the voxel and its cluster center. The formulae for calculating the value of D_l , D_{xyz} , D_w , and D_s are as follows (7-10):

$$D_l = \sqrt{(l_j - l_i)^2} \quad (7)$$

$$D_{xyz} = \sqrt{(x_j - x_i)^2 + (y_j - y_i)^2 + (z_j - z_i)^2} \quad (8)$$

$$D_w = \sqrt{(suv_j - suv_i)^2} \quad (9)$$

$$D_s = \frac{D_c + \alpha D_{xyz} + \beta D_w}{\sqrt{1 + \alpha^2 + \beta^2}} \quad (10)$$

Where i is the i -th supervoxel clustering center, j represents a voxel in the search area. α is a parameter used to adjust the weight of D_{xyz} , and β is a parameter used to adjust the weight of D_w .

The traditional two-dimensional region-growing method begins with one or several seed points or seed area; based on certain growth criteria, the neighborhood pixels in a two-dimensional image are assessed and connected until all the pixels are completely connected [9]. The region-growing method generally involves three main issues: the selection of the seed point, the growth criteria used, and the termination condition. The results of region-growing are directly related to these three issues.

3D region-growing methods [8] generally begin with the seed point and some manually chosen growth criteria, and the voxels' neighborhoods are merged into the seed areas that meet the growth criteria. For 2D image areas, the seed points have 4 or 8 neighborhoods. Seed points in 3D images generally have 6 or 26 neighborhoods, depending on whether diagonally adjacent points are included. The 3D region-growing method can provide three-dimensional adjacent voxel information. When this algorithm is used, all the data are placed into memory. However, a set of 3D lung image data is approximately 150 M in size, rendering the algorithm's calculation time and memory space requirements very large. A map of the neighborhood areas used in the 2D and 3D region-growing methods is shown in Figure 7.

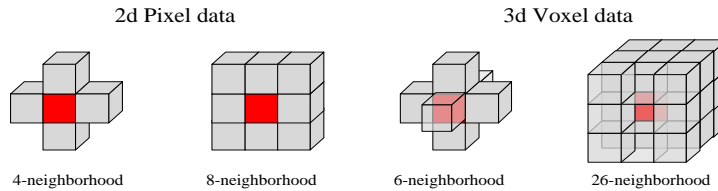


Figure 7. 2D and 3D region-growing algorithm seed point neighborhoods.

Compared with voxels, supervoxels preserve the boundary information of the original image and has statistical information relating to multiple voxels; therefore, supervoxels are rich in characteristic information and can greatly reduce the processing complexity of the subsequent images and improve the split speed of the image.

Based on the three-dimensional voxel-based region-growing method and supervoxels, we proposed an improved 3D region-growing method based on supervoxels and multimodal data. Using supervoxels as the basic unit and the sequence characteristics of nodules in sequence images enables the full use of information on SUV values in PET images. Automatic access to the seed point of supervoxels and growth in the field of seed 6-neighborhoods improves 3D supervoxel region growing according to the proposed similarity function (7-10), finally achieving the segmentation and reconstruction of the pulmonary nodule in sequence images.

The seed point we select is the point with the highest SUV value in the PET image; we obtain the coordinates (x, y) and the serial number z of the image and then take (x, y, z) as the seed point to automatically execute the improved supervoxel 3D region-growing method, which obeys the similarity function. This is then combined with information on the color, distance and SUV difference between supervoxels. According to the corresponding adjustment parameters, we then calculate the similarity between two supervoxels and incorporate supervoxels with similar properties into the seed area, which then serves as the new seed area. In this way, we continue searching for supervoxels in their 6-neighborhoods and merge similar voxels, thus growing the size of the seed area until it no longer changes. Finally, all supervoxels in the seed area are shown.

The steps of the improved supervoxel 3D region-growing algorithm are shown in Algorithm 2.

Algorithm 2 Improved supervoxel 3D region-growing algorithm

1. Select the point which has the highest SUV value in the PET image as the seed point;
2. Obtain the centroid coordinates (x, y) and the serial number z of the seed point;
3. Use the coordinates (x, y, z) as the supervoxels' growing seed point and mark it as a seed area;
4. According to the growing rules, search for supervoxels in the seed area's 6-neighborhood that have similar properties;
5. Incorporate supervoxels that have similar properties into the seed area, which then serves as the new seed area;
6. Repeat steps 3-4 until the seed area's size no longer changes;
7. Show all supervoxels in the seed area

3. Results and Discussion

The PET/CT image datasets used in this study were obtained from a hospital in Shanxi Province, China. All data can be accessed at <https://figshare.com/s/43e0acc1343ae3f5f77d>. We used a Discovery ST16 PET-CT scanner from the General Electric Company of America (150 mA, 140 kV, with a slice thickness of 3.75 mm). The size of each CT image was 512×512 , and the size of each PET image was 128×128 . In the experiment, we selected 256 lung CT and PET sequence image datasets containing a total of 609 nodule images. Based on the physician's knowledge and the morphological perspective of lung CT image sequences, the datasets were divided into four categories: solitary pulmonary nodules (203 nodules), pleural nodules (152 nodules), juxta-vascular nodules (147 nodules) and cavitary nodules (107 nodules). We invited two radiologists to perform manual segmentation for all pulmonary nodule sequence images for comparison.

3.1. Qualitative Evaluation

To verify our method's validity and universality for the pulmonary nodule segmentation of CT/PET image sequences, we compared the results obtained using our method with the 3D voxel-based region-growing (3D-RG) method and with manual segmentation performed by two experts.

3.1.1. Analyzing Contrast Effects in Different Nodules

With reference to the morphological classification of pulmonary nodules [17], we display four types of pulmonary nodule segmentation result: solitary pulmonary nodules (SPNs), pleural nodules (PNs), juxta-vascular nodules (JNs) and cavitary nodules (CNs). Because the number of image sequences is too large, we chose 5 images from the top of the lung to the bottom of the lung in lung CT images to show the process of image segmentation and its results: one image showing the top of the lung, one image showing the bottom of the lung, and three images showing pulmonary nodules. Because we found no nodules at the top or bottom of the lung, there are no experimental results for the first and fifth lines in columns (b), (e) and (f).

Our method for SPNs, PNs, JNs, CNs segmentation is shown in Figure 8, Figure 9, Figure 10 and Figure 11. For SPNs, CNs, PNs, JNs reconstruction is shown in Figure 12, Figure 13, Figure 14 and Figure 15.

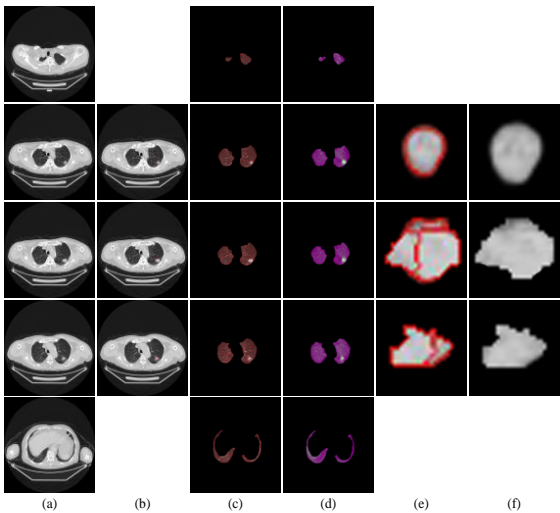


Figure 8. Segmentation results for SPNs. Column (a) shows the original CT images from top to bottom;(b) shows the manual segmentation result; (c) shows the superpixel segmentation result for lung parenchyma; (d) shows the MI registration result in PET/CT on (c); and (e) and (f) show the superpixels and final results for SPNs.

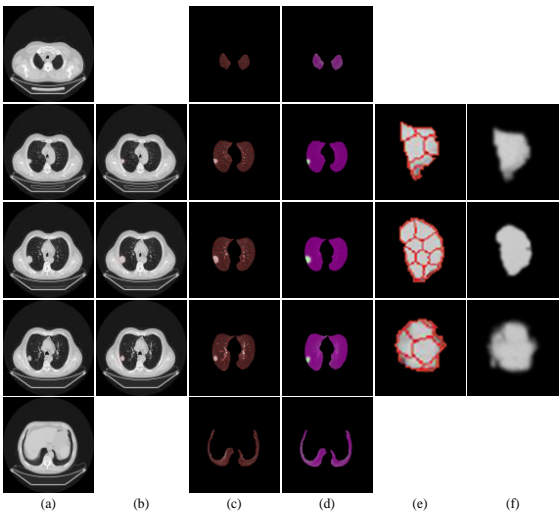


Figure 9. Segmentation results for PNs. Column (a) shows the original CT images from top to bottom;(b) shows the manual segmentation result; (c) shows the superpixel segmentation result for lung parenchyma; (d) shows the MI registration result in PET/CT on (c); and (e) and (f) show the superpixels and final results for PNs.

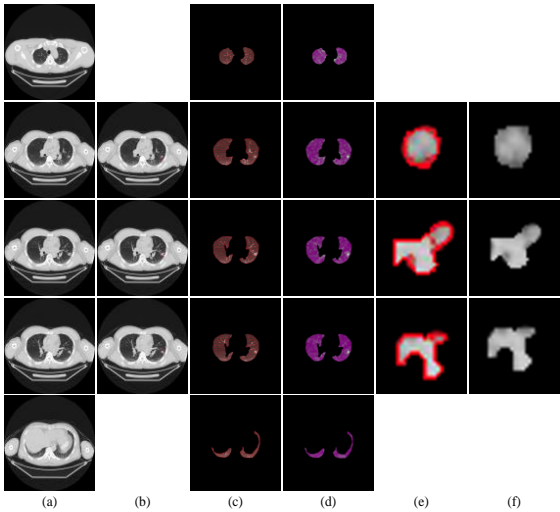


Figure 10. Segmentation results for JNs. Column (a) shows the original CT images from top to bottom;(b) shows the manual segmentation result; (c) shows the superpixel segmentation result for lung parenchyma; (d) shows the MI registration result in PET/CT on (c); and (e) and (f) show the superpixels and final results for JNs.

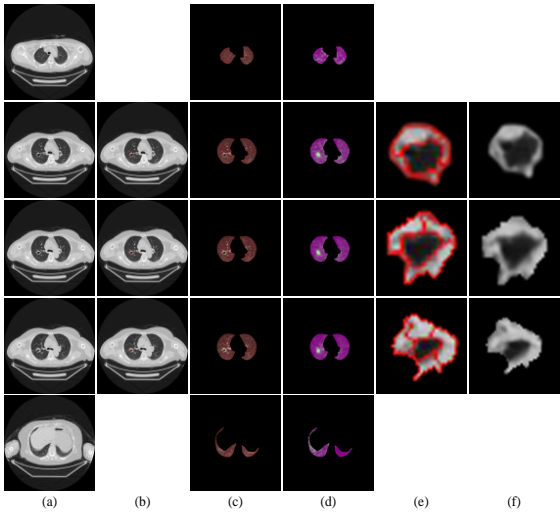


Figure 11. Segmentation results for CNs. Column (a) shows the original CT images from top to bottom;(b) shows the manual segmentation result; (c) shows the superpixel segmentation result for lung parenchyma; (d) shows the MI registration result in PET/CT on (c); and (e) and (f) show the superpixels and final results for CNs.



Figure 12. The reconstruction result for SPNs obtained using our method; (a) and (b) show different perspectives of the pulmonary nodule reconstruction results.

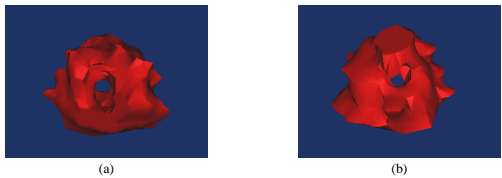


Figure 13. The reconstruction results for CNs obtained using our proposed method; (a) and (b) show different perspectives of the CN reconstruction results.

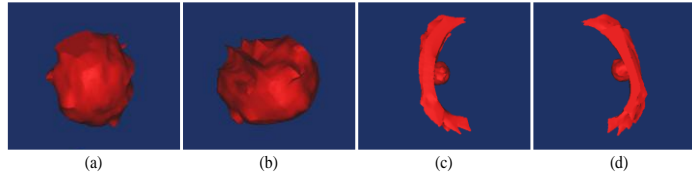


Figure 14. The reconstruction results for PNs obtained using our method; (a) and (b) show different perspectives of the nodule reconstruction results; (c) and (d) show some pleural environments for PNs from different perspectives.

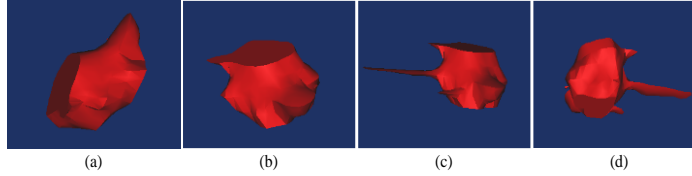


Figure 15. The reconstruction results for JNs obtained using our method; (a) and (b) show different perspectives of the pulmonary nodule reconstruction results; (c) and (d) shown some vascular environments for JNs from different perspectives.

The results showed that for the four kinds of lung lesions, compared with the artificial segmentation result, our method provided good segmentation results. Not only for SPNs but also for PNs, JNs and CNs (three types of irregular pulmonary nodules), very good segmentation results were obtained. Furthermore, our method can ensure the integrity of the segmentation for pulmonary nodule images because our method provided a better segmentation effect and versatility.

3.1.2. Comparison with the 3D-RG Method

The average numbers of voxels and supervoxels for four types nodules are shown in Table 1.

Table 1. The average numbers of voxels and supervoxels for four nodule types

Type	CT [voxel]	Lung area VOI [voxel]	nodule area VOI [voxel]	nodule area VOI [supervoxel]
SPNs	512×512×299	512×512×75	33×27×11	15×13×6
PNs	512×512×299	512×512×82	34×28×10	16×13×5
JNs	512×512×287	512×512×77	45×60×15	21×29×9
CNs	512×512×287	512×512×78	36×37×12	17×16×7

The growing results of pulmonary nodules obtained using 3D-RG are displayed in green, and the growing results obtained using the method we propose are displayed in red. We set the opacity of the 3D-RG results to 1 (completely opaque), the opacity of the growing results obtained using our method to 0.5 (translucent), and combined the two results as shown in the figure below.

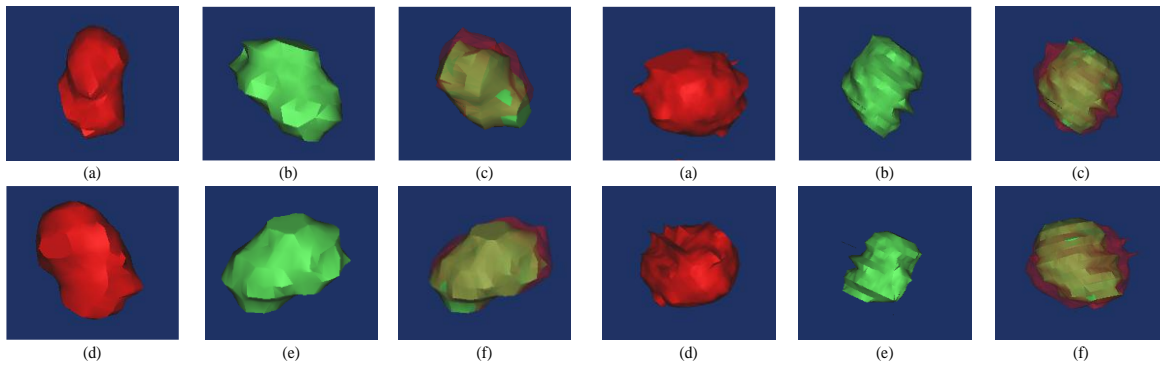


Figure 16. The comparison for SPNs; (a) and (d) are different perspectives of the results obtained using our method for SPNs; (b) and (e) are different perspectives of the results obtained using 3D-RG for SPNs; and (c) and (f) are the results obtained by setting the opacity for the two methods.

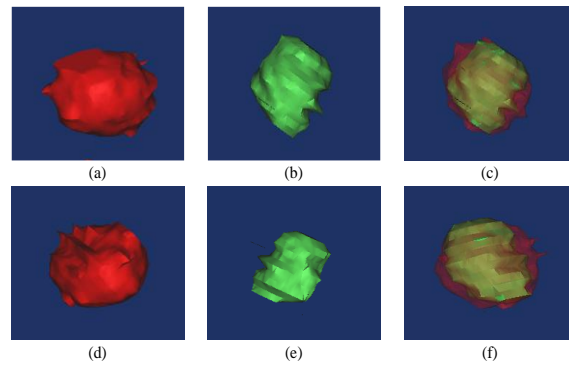


Figure 17. The comparison for PNs; (a) and (d) are different perspectives of the results obtained using our method for SPNs; (b) and (e) are different perspectives of the results obtained using 3D-RG for PNs; and (c) and (f) are the results obtained by setting the opacity for the two methods.

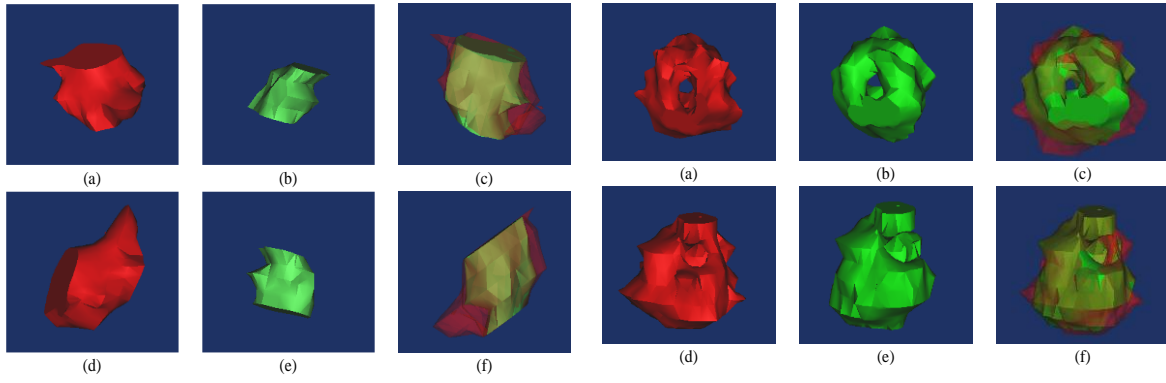


Figure 18. The comparison for JNs; (a) and (d) are different perspectives of the results obtained using our method for SPNs; (b) and (e) are different perspectives of the results obtained using 3D-RG for JNs; and (c) and (f) are the results by setting the opacity for two methods.

Figure 19. The comparison for CNs; (a) and (d) are different perspectives of the results obtained using our method for SPN; (b) and (e) are different perspectives of the results obtained using 3D-RG for CNs and (c) and (f) are the results by setting the opacity for two methods.

The reconstruction results for SPNs, PNs, JNs, CNs obtained using the two methods are shown in Figure 16, Figure 17, Figure 18, Figure 19.

According to the contrast experiment result, our method is better than 3D-RG because it not only has a great advantage in terms of time complexity, but also provides better growing results. 3D-RG cannot describe the nodules surface information correctly. However, we combined supervoxels with the SUV information encoded in PET images, and the supervoxels provided good results in terms of retaining the boundary of the pulmonary nodules; thus, SUV information can reflect the pulmonary nodule metabolic information, and when combined, the two methods can grow pulmonary nodules correctly.

3.2. Qualitative Evaluation

The Jaccard similarity coefficient [26], relative volume difference [14] and time complexity are used to objectively assess the performance of the proposed algorithm.

Table 2 shows the average scores of the Jaccard, RVD and time complexity measures for our method and 3D-RG for the four types of nodules in the data set.

Table 2. Average values of Jaccard, RVD, and Time complexity for our method and 3D-RG for the four types of pulmonary nodules

Type	Dataset size	Measures	Our method	3D-RG
SPNs	512×512×75	Jaccard	97.18%	77.69%
		RVD	3.11%	22.31%
		Running Time	182.06s	192.65s
PNs	512×512×82	Jaccard	94.99%	76.90%
		RVD	5.27%	-23.10%
		Running Time	197.38	221.59
JNs	512×512×77	Jaccard	91.06%	52.28%
		RVD	-8.94%	-65.33%
		Running Time	202.44	196.57
CNs	512×512×78	Jaccard	98.86%	81.76%
		RVD	1.16%	-18.24%
		Running Time	180.32	191.65

3.2.1. Jaccard Similarity Coefficient

The Jaccard similarity coefficient is used to compare the similarity between sample sets, which can indicate the degree of overlap of two voxel sets [26]. The Jaccard coefficient can be calculated according to (11). The Jaccard similarity coefficient shows the overlap between the artificial segmentation result and the computer segmentation result.

$$Jaccard = \frac{A \cap B}{A \cup B} \quad (11)$$

Jaccard values lie in the range [0, 1], and a higher Jaccard similarity coefficient indicates a better segmentation result. A represents the volume of the computer segmentation result, and B represents the volume of the artificial segmentation result.

The comparison of the Jaccard similarity coefficients for the datasets using our method and 3D-RG is shown in Table 2 and Figure 20; yellow squares represent SPNs, red circles represent JNs, green triangles represent PNs, and blue diamonds represent CNs.

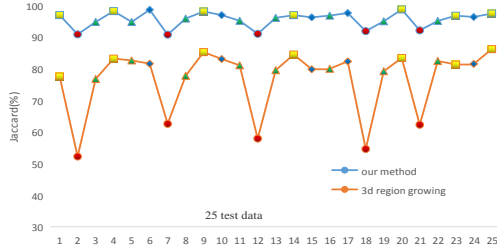


Figure 20. Jaccard curves for the two algorithms

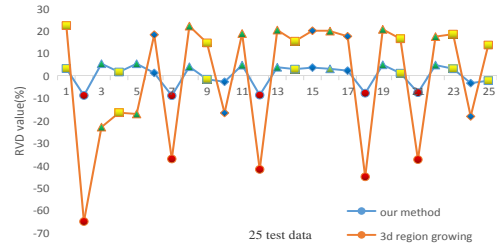


Figure 21. RVD curves for the two algorithms.

From Figure 20, we can conclude that for different types of pulmonary nodules, our method performs better than 3D-RG. For SPNs, our method provides better segmentation and reconstruction. Jaccard similarity coefficients were more than 97%. The highest value was 98.97%, almost the same as that obtained using artificial segmentation. However, the highest Jaccard value obtained for SPNs using 3D-RG was only 86.37%. For PNs, our method also provided a better result. Compared with SPNs, the Jaccard similarity coefficient decreased slightly but remained higher than 95%, and the highest value reached 97.02%. However, the highest Jaccard value obtained for PNs using 3D-RG was only 82.78%. For JNs, the performance of our method was slightly lower, but the Jaccard similarity coefficient remained higher than 90%. The highest value reached 92.33%. However, the highest Jaccard value obtained for JNs using 3D-RG was only 62.66%, a poor performance. For CNs, our method exhibited a good performance; the Jaccard similarity coefficient reached higher than 96%, up to 98.86%. However, the highest Jaccard value obtained for CNs using 3D-RG was only 82.23%.

3.2.2. Relative Volume Difference

Relative volume difference describes the degree of undersegmentation or oversegmentation [14]. The relative volume difference between two sets of voxels is given in percent and is defined as in (12); A is used for segmentation and B is used as a reference. A value of 0 means that both volumes are identical. Note that this does not imply that the tumors are identical or actually overlap. For this reason, the relative volume difference should never be used as the only measure of segmentation quality. However, in combination with other measures, this parameter reveals if a method tends to over- or under-segment. For this reason, the results of the relative volume difference are given as signed numbers. To calculate the corresponding score, the absolute value is used. When the result is positive, oversegmentation (over-seg) occurs, and when the result is negative, undersegmentation (under-seg) occurs. This measure not only distinguishes between over- and undersegmentation but also directly evaluates volumetric information. During nodule segmentation, information on nodule volume is very important.

$$RVD = 100 \left(\frac{|A| - |B|}{|B|} \right) \quad (12)$$

The comparison of the RVD results for the datasets using our method and 3D-RG is shown in Table 2. The nodule segmentation result (RVD curves) for datasets using the two methods is shown in Figure 21.

From Figure 21, we can conclude that the degree of the over- and undersegmentation obtained using our method is significantly lower than that obtained using 3D-RG. For SPNs, our method provides better segmentation and reconstruction.

For the RVD coefficient for SPNs, the highest value of over-seg was 3.11%, and the highest value of under-seg was 2.32%; the average RVD value was 2.22%. However, the average RVD value obtained using 3D-RG reached 16.78%, and good performance was not achieved. For PNs, our method also provided a better result. The highest value of over-seg was only 5.27%, and there was no under-seg; the average RVD value was 4.40%. Demonstrably, our method exhibited good performance in PNs. However, the average RVD value obtained using 3D-RG reached 19.92%, representing poor performance. For JNs, the performance of our method declined slightly, but the RVD coefficient remained at 10%. The highest value of under-seg was 9.03%, and no over-seg occurred; the average RVD value was 8.47%. However, the average RVD value obtained using 3D-RG was 45.53%, representing poor performance. For CNs, the highest value of over-seg obtained using our method was 3.53%, the highest value of under-seg was 3.42%, and the average RVD value was 2.62%. However, the average RVD value obtained when using 3D-RG was 18.17%, representing poor performance.

3.2.3. Time Complexity

We also analyzed the time performance of the two methods for four types of nodule images (Table 2), and the average processing times for the four types of nodules obtained using our method and 3D-RG are shown in Figure 22.

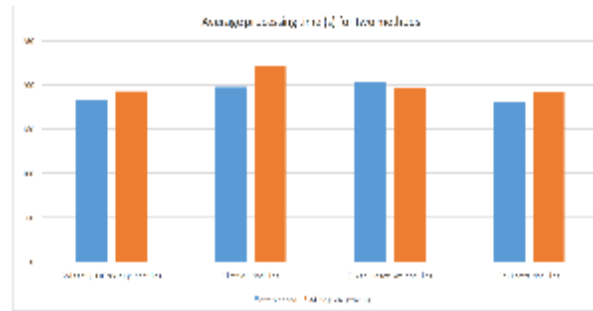


Figure 22. The average processing time of two methods

As shown in Figure 22, for four types of nodules, the processing time required by our method is approximately the same as that of 3D-RG and sometimes slightly better than that of 3D-RG. Because of the growth criteria used to analyze PET images, calculating the value of SUV requires long times. 3D-RG uses voxel as the basic unit to process datasets while our method use supervoxel as the basic unit. Supervoxels can combine the statistical information associated with many voxels and keep the boundary and feature information in original image, thus greatly reducing the running time of the program Table 2 and Figure 22 show that the average processing time of our algorithm is 190.55 s, and the average processing time of 3D-RG is 200.62 s. That is, it will take 2.44 s to process a single case using our method, which is faster than the processing time of 3D-RG (2.57 s). As a result, our method is slightly better than 3D-RG in terms of the speed of segmentation and the reconstruction of nodule images.

4. Conclusions

In this paper, we propose a new automatic algorithm for the segmentation and reconstruction of pulmonary nodules; this algorithm exhibits good results for solitary pulmonary nodules, pleural nodules, juxta-vascular nodules and cavitary nodules. The experimental results show that our method can achieve accurate segmentation and reconstruction of the pulmonary nodules in lung lesions, and these results are of especially high quality for pulmonary nodules, which have complex morphological structures, such as pleural nodules, juxta-vascular nodules and cavitary nodules. Compared with the 3D region-growing method, our method is more accurate and more universally applicable; the average segmentation time required for each case when using our method is 190.55 s. These results are superior to the voxel-based 3D region-growing method. Our method can achieve an average volume voxel overlap ratio of $94.97 \pm 4.00\%$ for the four types of pulmonary nodules image sequences, much better than the 3D region-growing method. Thus, our method is an efficient and accurate method for the segmentation and reconstruction of pulmonary nodules.

Acknowledgements

This research is supported by the National Natural Science Foundation of China (61373100); the Virtual Reality Technology and System National Key Laboratory of Open Foundation (BUAA-VR-16KF-14); the Virtual Reality Technology and System National Key Laboratory of Open Foundation (BUAA-VR-16KF-15); and the Research Project Supported by Shanxi Scholarship Council of China (2016-038).

References

1. F. Behnia, S. Elojeimy, M. Matesan, and D. C. Fajgenbaum, "Potential Value of FDG PET-CT in Diagnosis and Follow-up of TAFRO Syndrome," *Annals of Hematology*, vol. 96, no. 3, pp. 497–500, March 2017
2. W. D. Bidgood, S. C. Horii, F. W. Prior, and D. E. V. Syckle, "Understanding and Using DICOM, the Data Interchange Standard for Biomedical Imaging," *Journal of the American Medical Informatics Association Jamia*, vol. 4, no. 3, pp. 199–212, 1997
3. R. Brunelli, "Template Matching Techniques in Computer Vision: Theory and Practice", Wiley Publishing Co., Inc., Hoboken, 2009
4. A. K. Buck and M. Schwaiger, "Positron Emission Tomography," Springer Berlin Heidelberg Co., Inc., Berlin, 2017
5. Y. Chen, A. Furukawa, A. Taniguchi, T. Tateyama, and S. Kanasaki, "Automated Assessment of Small Bowel Motility Function based on Simple Linear Iterative Clustering (SLIC)," in *Proceedings of the 12th International Conference on Fuzzy Systems and Knowledge Discovery (FSKD)*, pp.1737-1740, Zhangjiajie, China, August 2015
6. J. H. Chu, H. Min, L. Liu, and W. Lu, "A Novel Computer Aided Breast Mass Detection Scheme based on Morphological Enhancement and SLIC Superpixel Segmentation," *Medical Physics*, vol. 42, no. 7, pp. 3859–3869, July 2015
7. S. Diederich, M. Lentschig, T. Overbeck, D. Wormanns, and W. Heindel, "Detection of Pulmonary Nodules at Spiral CT: Comparison of Maximum Intensity Projection Sliding Slabs and Single-image Reporting," *European Radiology*, vol. 11, no. 8, pp. 1345–1350, August 2001
8. A. Fabijańska, M. Janaszewski, M. Postolski, L. Babout, "Airway Tree Segmentation from CT Scans Using Gradient-Guided 3D Region Growing," in *Proceedings of the 14th Iberoamerican Conference on Pattern Recognition: Progress in Pattern Recognition, Image Analysis, Computer Vision, and Applications (CIARP)*, pp. 247–254, Guadalajara, Jalisco, Mexico, November 2009
9. H. P. Fan, G. H. Zeng, M. Body, and M. S. Hacid, "Seeded Region Growing: an Extensive and Comparative Study," *Pattern Recognition Letters*, vol. 26, no. 8, pp. 1139–1156, June 2005
10. A. A. Farag, J. Graham, S. Elshazly, and A. Farag, "Data-driven Lung Nodule Models for Robust Nodule Detection in Chest CT," in *Proceedings of the 20th International Conference on Pattern Recognition (ICPR)*, pp. 2588–2591, Istanbul, Turkey, August 2010
11. G. H. Gu and Y. Zhao, "Scene Classification based on Spatial Pyramid Representation by Superpixel Lattices and Contextual Visual Features," *Optical Engineering*, vol. 51, no. 1, pp. 7201–7209, February 2012
12. A. A. Hammoudi, F. Li, L. Gao, Z. Wang, M. J. Thrall, and Y. Massoud, "Automated Nuclear Segmentation of Coherent Anti-stokes Raman Scattering Microscopy Images by Coupling Superpixel Context Information with Artificial Neural Networks," in *Proceedings of the Second International Conference on Machine Learning in Medical Imaging (MLMI)*, pp. 317–325, Toronto, Canada, September 2011
13. D. M. Hansell, A. A. Bankier, H. MacMahon, T. C. McLoud, N. L. Müller, and J. Remy, "Fleischner Society: Glossary of Terms for Thoracic Imaging," *Radiology*, vol. 246, no. 3, pp. 697–722, March 2008
14. T. Heimann, B. van Ginneken, M. A. Styner, Y. Arzhaeva, V. Aurich, and C. Bauer, "Comparison and Evaluation of Methods for Liver Segmentation from CT Datasets," *IEEE Transactions on Medical Imaging*, vol. 28, no. 8, pp. 1251–1265, August 2009
15. B. Irving, A. Cifor, B. W. Papiez, J. Franklin, E. M. Anderson, S. M. Brady, and J. A. Schnabel, "Automated Colorectal Tumour Segmentation in DCE-MRI Using Supervoxel Neighbourhood Contrast Characteristics," in *Proceedings of the International Conference on Medical Image Computing and Computer-Assisted Intervention (MICCAI)*, pp. 609–616, Boston, USA, September 2014
16. S. Kobashi, N. Kamiura, Y. Hata, and F. Miyawaki, "Volume-quantization-based Neural Network Approach to 3D MR Angiography Image Segmentation," *Image & Vision Computing*, vol. 19, no. 4, pp. 185–93, March 2001
17. W. J. Kostis, A. P. Reeves, D. F. Yankelevitz, and C. I. Henschke, "Three-dimensional Segmentation and Growth-rate Estimation of Small Pulmonary Nodules in Helical CT Images," *IEEE Transactions on Medical Imaging*, vol. 22, no. 10, pp. 1259–1274, October 2003
18. X. L. Liao, J. J. Zhao, C. Jiao, L. Lei, Y. Qiang, and Q. Cui, "A Segmentation Method for Lung Parenchyma Image Sequences based on Superpixels and a Self-Generating Neural Forest," *Plos One*, vol. 11, no. 8, pp. e0160556, August 2016
19. Y. Lin and C. Xiu, "Template Matching Algorithm Based on Edge Detection," in *Proceedings of the International Symposium on Computer Science and Society (ISCCS)*, pp. 7–9, Kota Kinabalu, Malaysia, July 2011
20. M. Liu, O. Tuzel, S. Ramalingam, and R. Chellappa, "Entropy Rate Superpixel Segmentation," in *Proceedings of the 2011 IEEE Conference on Computer Vision and Pattern Recognition (CVPR)*, pp. 2097–2104, Colorado Springs, USA, June 2011
21. H. Luan, F. Qi, Z. Xue, L. Chen, and D. Shen, "Multimodality Image Registration by Maximization of Quantitative-qualitative Measure of Mutual Information," *Pattern Recognition*, vol. 41, no. 1, pp. 285–98, January 2008
22. L. B. Lusted, "Logical Analysis in Roentgen Diagnosis," *Radiology*, vol. 74, no. 2, pp. 178–193, February 1960
23. F. Maes, A. Collignon, D. Vandermeulen, and G. Marchal, "Multi-modality Image Registration by Maximization of Mutual Information," *IEEE Transactions on Medical Imaging*, vol. 16, no. 2, pp. 187–198, May 1997
24. P. Masa-Ah and S. Soongsathitanon, "A Novel Standardized Uptake Value (SUV) Calculation of PET DICOM Files Using MATLAB," in *Proceedings of the 10th WSEAS International Conference on Applied Informatics and Communications, and 3rd WSEAS International Conference on Biomedical Electronics and Biomedical Informatics (AIC/BEBI)*, pp. 413–416, Taipei, Taiwan, August 2010
25. A. Moore, S. Prince, J. Warrell, U. Mohammed, and G. Jones, "Superpixel Lattices," in *Proceedings of the 2008 IEEE Conference on Computer Vision and Pattern Recognition (CVPR)*, pp. 1–8, Anchorage, USA, June 2008
26. M. Prastawa, E. Bullitt, S. Ho, and G. Gerig, "A Brain Tumor Segmentation Framework based on Outlier Detection," *Medical Image Analysis*, vol. 8, no. 3, pp. 275–283, September 2004

27. X. Ren and J. Malik, "Learning a Classification Model for Segmentation," in *Proceedings of the Ninth IEEE International Conference on Computer Vision (ICCV)*, pp. 10, Washington DC, USA, October 2003
28. C. Revol-Muller, F. Peyrin, Y. Carrillon, and C. Odet, "Automated 3D Region Growing Algorithm based on an Assessment Function," *Pattern Recognition Letters*, vol. 23, no. 1-3, pp. 137-150, January 2002
29. R. Siegel, D. Naishadham, and A. Jemal, "Cancer statistics, 2013," *CA: A Cancer Journal for Clinicians*, vol. 63, no. 1, pp. 11-30, January 2013
30. S. S. Sun, Y. Guo, Y. B. Guan, H. Z. Ren, L. N. Fan, and Y. Kang, "Juxta-vascular Nodule Segmentation based on Flow Entropy and Geodesic Distance," *IEEE Journal of Biomedical & Health Informatics*, vol. 18, no. 4, pp. 1355-1362, July 2014
31. W. J. Tuddenham, "Visual Search, Image Organization, and Reader Error in Roentgen Diagnosis. Studies of the Psychophysiology of Roentgen Image Perception," *Radiology*, vol. 78, no. 5, pp. 694-704, May 1962
32. P. Viola and W. M. W. Iii, "Alignment by Maximization of Mutual Information," *International Journal of Computer Vision*, vol. 24, no. 2, pp. 137-54, September 1997
33. T. W. Way, L. M. Hadjiiski, B. Sahiner, H. P. Chan, and P. N. Cascade, "Computer-aided Diagnosis of Pulmonary Nodules on CT Scans: Segmentation and Classification Using 3D Active Contours," *Medical Physics*, vol. 33, no. 7, pp. 2323-2337, July 2006
34. S. Wu and J. Wang, "Pulmonary Nodules 3D Detection on Serial CT Scans," in *Proceedings of the Second WRI Global Congress on Intelligent Systems (GCIS)*, pp. 257-260, Wuhan, China, November 2012
35. W. Wu, Z. Zhou, S. Wu, and Y. Zhang, "Automatic Liver Segmentation on Volumetric CT Images Using Supervoxel-based Graph Cuts," *Computational and Mathematical Methods in Medicine*, vol. 2016, no. 2016-4-5, pp. 2016:9093721, April 2016

Qiang Cui received his BD in software engineering from the Taiyuan University of Technology in 2015. He is currently pursuing his MD in the area of medical image processing at Taiyuan University of Technology (TYUT).

Zilin Qiang is currently pursuing his BD in the area of software engineering at TYUT.

Juanjuan Zhao is a Professor at the School of Computer Science and Technology at TYUT, China. She received her PhD in Computer Application Technology from TYUT in 2010. Her current research interests are in medical image processing and the Internet of Things.

Yan Qiang received his PhD in Computer Application Technology from TYUT in 2010. He is a Professor at the School of Computer Science and Technology, TYUT, China. His current research topics include image processing and cloud computing.

Xiaolei Liao received his BD in Computer Science and Technology from the Taiyuan University of Technology in 2014. He received his MD in Computer Science and Technology from the Taiyuan University of Technology in 2017.